Electrostatic analyzer with a 3-D instantaneous field of view for fast measurements of plasma distribution functions in space

Xavier Morel, Matthieu Berthomier, Jean-Jacques Berthelier

Key Points:
- An electrostatic analyzer with an instantaneous 3-D field of view is optimized to combine high geometric factor and efficient UV rejection
- The 3-D plasma analyzer covers energies from few eV to 30 keV with 7 to 10% energy resolution and 3 to 12 degrees angular resolution
- The proposed instrument has 192 entrance windows corresponding to eight polar channels and 24 azimuthal sectors

Correspondence to:
M. Berthomier,
matthieu.berthomier@lpp.polytechnique.fr

Electrostatic analyzer with a 3-D instantaneous field of view for fast measurements of plasma distribution functions in space

X. Morel[1,2], M. Berthomier[1,2], and J.-J. Berthelier[3,4] (iD)

[1]Laboratoire de Physique des Plasmas, Ecole Polytechnique, Palaiseau, France, [2]Sorbonne Universités, UPMC, CNRS UMR 7648, Paris, France, [3]Laboratoire Atmosphères, Milieux, Observations Spatiales, UVSQ, Guyancourt, France, [4]Sorbonne Universités, UPMC, CNRS UMR 8190, Paris, France

Abstract We describe the concept and properties of a new electrostatic optic which aims to provide a 2π sr instantaneous field of view to characterize space plasmas. It consists of a set of concentric toroidal electrodes that form a number of independent energy-selective channels. Charged particles are deflected toward a common imaging planar detector. The full 3-D distribution function of charged particles is obtained through a single energy sweep. Angle and energy resolution of the optics depends on the number of toroidal electrodes, on their radii of curvature, on their spacing, and on the angular aperture of the channels. We present the performances, as derived from numerical simulations, of an initial implementation of this concept that would fit the need of many space plasma physics applications. The proposed instrument has 192 entrance windows corresponding to eight polar channels each with 24 azimuthal sectors. The initial version of this 3-D plasma analyzer may cover energies from a few eV up to 30 keV, typically with a channel-dependent energy resolution varying from 10% to 7%. The angular acceptance varies with the direction of the incident particle from 3° to 12°. With a total geometric factor of two sensor heads reaching ~0.23 cm^2 sr eV/eV, this "donut" shape analyzer has enough sensitivity to allow very fast measurements of plasma distribution functions in most terrestrial and planetary environments on three-axis stabilized as well as on spinning satellites.

1. Introduction

1.1. Need of 3-D Plasma Measurements in Space Physics

In most space plasmas, including terrestrial and planetary magnetospheres and in the solar wind, the distribution function of charged particles has to be measured at high time resolution—typically a few tens of milliseconds—in order to understand the dynamical phenomena that occur in these complex environments [see, e.g., *Berthomier et al.*, 2012]. This is the task of plasma analyzers which cover the so-called thermal energy range from a few eV up to ~30 keV. The principles of electrostatic optics are used to design these instruments which first select and then detect charged particles of a given energy per charge [*Dahl*, 1973]. Sweeping of the voltage applied to the electrodes of the electrostatic optics is required to obtain the complete particle energy per charge spectrum.

In magnetized plasmas, it is also most important to identify any anisotropy of the charged particles distribution function. Such out-of-equilibrium properties of the local plasma reveal acceleration and/or heating processes [*Baumjohann and Treumann*, 1996], and it is of particular importance to determine the angular distribution of charged particles relative to the local terrestrial or planetary magnetic field direction which defines the so-called pitch angle distribution of charged particles. In many circumstances, the mean direction of the magnetic field is highly variable. This is the case in regions where magnetic reconnection occurs (e.g., at the Earth's magnetopause), in the inner heliosphere where turbulent magnetic fields are observed, and in many other active regions such as planetary bow shocks and magnetotails [*Kivelson and Russel*, 1995]. The field of view (FOV) of space plasma analyzers must therefore cover as much of 4π sr as possible in order to constantly encompass the magnetic field direction. Measuring both the energy spectrum and the 3-D pitch angle distribution at high time resolution remains one of the main challenges of modern space plasma instrumentation [*Young*, 1998].

1.2. State-of-the-Art 2-D Plasma Analyzers

Since the early 1980s, most space plasma analyzers that have been implemented on space missions are based on the "top-hat" design first developed by *Carlson et al.* [1985] and schematically shown in Figure 1.
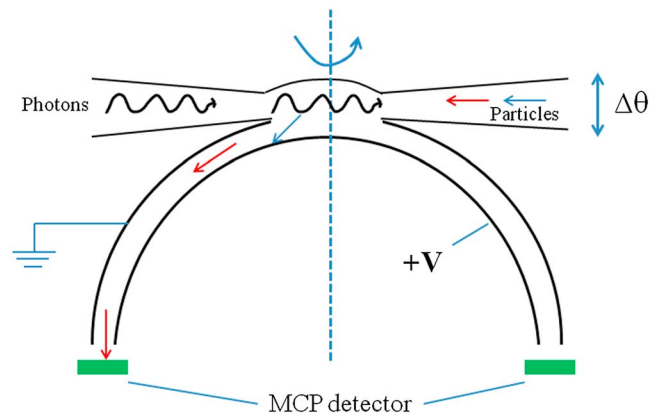
Figure 1. Schematics of the top-hat plasma analyzer which exhibits an axial symmetry and provides a 2-D field of view.

Particles enter the instrument through a collimated entrance which limits the direct access of UV photons to the inner part of the optics. High-voltage biased concentric hemispherical electrodes are focusing particles with the appropriate energy per charge ratio toward the instrument detector, usually a set of microchannel plates (MCPs) [*Wiza*, 1979] that form a circular crown in the plane perpendicular to the symmetry axis of the instrument. The spacing of the electrodes determines the energy band pass of the optics. Localization of the electron cloud issued from the MCP and collected by an anode underneath allows determining the direction of incoming particles. Major recent space science missions including Active Magnetospheric Particle Tracer Explorers/Ion Release Module [*Paschmann et al.*, 1985], FAST [*Carlson et al.*, 2001], Cassini [*Linder et al.*, 1998], Cluster [*Johnstone et al.*, 1997], and Time History of Events and Macroscale Interactions during Substorms [*McFadden et al.*, 2008] used this flight-proven analyzer concept. Despite its reliability and robustness, it presents strong limitations because of its restricted 2-D FOV, generally $180° \times \Delta\varphi$ or $360° \times \Delta\varphi$ where the polar acceptance $\Delta\varphi$ is of the order of 5°.

Coverage of the whole phase space is possible on spin-stabilized satellites since the instrument 2-D FOV scans directions while the satellite is rotating around its spin axis. With an intrinsic $360° \times \Delta\varphi$ FOV, the 3-D distribution function of charged particles (either ions or electrons) can be obtained every satellite half spin period. One may think that the temporal resolution of the measurements can be improved by decreasing the spin period of the satellite to a fraction of a second. However, satellites dedicated to the study of space plasma physics phenomena need to make reliable measurements of the 3-D electric field. This is crucial to identify electric fields that are parallel to the static magnetic field and often play a key role in particle acceleration processes [see *Marklund*, 2009, and references therein]. The measurement of the spin axis component of the DC electric field requires antennas that are deployed at the tip of long rigid booms [*Ergun et al.*, 2016]. The limited stiffness of these deployable structures and stability constraints of the satellite itself do not allow spin period below a few seconds typically [*Angelopoulos*, 2008].

In an attempt to maximize the FOV of plasma analyzers, *Vaisberg et al.* [1997] introduced the idea of electrostatic scanning for the slowly spinning Interball Tail spacecraft: an electrostatic scanner was installed in front of a toroidal analyzer. Each one of the two SCA-1 sensors provided a FOV extending about 70° from the main axis of the analyzer with 32 entrance windows and covered the 50 eV to 5 keV energy range in 7.5 s.

For three-axis stabilized (i.e., nonspinning) spacecraft, like STEREO which is continuously imaging the Sun, an alternative strategy is required to measure solar wind electrons: the solar wind electron analyzer (SWEA) instrument on board STEREO includes an electrostatic deflector consisting of two biased electrodes symmetrically located just before the entrance of the top-hat analyzer in order to sweep polar angles in a range of about ±60° [*Sauvaud et al.*, 2008]. The energy range of the instrument is limited by the need of higher voltages on the deflector electrodes since their distance is much larger than the gap between hemispherical electrodes of the top-hat energy analyzer. While the 3 keV upper limit of the SWEA instrument meets the requirement of electron measurements in the solar wind, this is not high enough in magnetospheres where tens of keV particles are common. The fast sweep of the deflector polarization also significantly increases power consumption of the instrument, and the time resolution of 3-D measurements is limited to a few seconds. More recently, *Desai et al.* [2015] developed an ion composition experiment that included a deflection system working in the range of ±45° between 10 eV/q and 40 keV/q.

On the four spacecraft MMS mission [*Burch et al.*, 2016] the spin axis component of the electric field is measured with a long axial antenna and the satellite spin period is 20 s. This allows an accurate measurement of the electric field vector, but, as a consequence, MMS science objectives, which target the highly dynamical magnetic

reconnection processes, require the use of eight half top-hat plasma analyzers with $180° \times \Delta\theta$ FOV for both electrons and ions. In addition, each sensor includes deflectors that perform the ultrafast sweep of polar angles over ±22°. They allow the 3-D coverage of electron phase space, up to ~30 keV, in 30 ms [*Pollock et al.*, 2016]. The same approach is used to measure the 3-D ion distribution function in 150 ms. However, this measurement strategy can hardly be extended to the next generation of large constellation missions [see, e.g., *Horbury et al.*, 2006] since it dramatically increases both the number of sensors and the resources needed on each satellite. An alternative technique studied by *Bedington et al.* [2014] consists in using a large number of 2-D FOV highly miniaturized plasma spectrometer whose design is well suited to microfabrication. This would in principle allow for simultaneous high time resolution analysis of electrons and ions distribution functions.

1.3. Limitations of Existing 3-D Plasma Analyzer Concepts

Only a few 3-D FOV plasma analyzer concepts have been proposed and developed in the past. The DYnamics of the Martian IOnosphere and Fast Omni-directional Non-scanning Energy Mass Analyser instruments on board the MARS 96 satellite were ion mass spectrometers with 3-D FOV capabilities on a three-axis stabilized platform [*Berthelier et al.*, 1998; *James et al.*, 1998]. However, DYMIO was designed for thermal ions below 700 eV and it only provided a coarse coverage of phase space with 32 independent entrance windows. FONEMA, which was coupling an electrostatic mirror with a Thomson parabola analyzer, was sampling ion phase space with 36 entrance windows between 20 eV and 8 keV in 125 ms.

The HYDRA instrument on the Polar spacecraft was a collection of cylindrical electron and ion analyzers for particles in the 2 eV–35 keV energy range [*Scudder et al.*, 1995]. It provided a sparse sampling of phase space with only 12 entrance windows. Typical time resolution was limited to half a second.

More recently, another attempt has been made with the Planetary Ion CAMera optical concept which works as an all-sky camera and uses electrostatic mirrors [*Vaisberg et al.*, 2005]. PICAM has a truly 3-D instantaneous FOV, but the voltages applied to the mirrors have to be equal to the particle's energy. Hence, this design is not suited to the study of tens of keV magnetospheric populations which would require exceedingly high polarization voltages. On board the Bepi-Colombo satellite, an optimized version of the original PICAM optical concept has an energy limit of 3 keV with maximal 8 s time resolution and $60° \times 15°$ angular resolution [*Orsini et al.*, 2010]. Although this instrument also includes an online time-of-flight system to determine the mass of the detected particles, its too small sensitivity does not allow high time resolution measurements needed by many space plasma physics objectives.

This short overview highlights the fact that to the best of our knowledge, no solution has been found so far to obtain high time resolution 3-D plasma measurements with a limited number of sensors, i.e., with power and mass resources compatible with the constraints of a constellation mission dedicated to the multiscale study of Sun-Earth interaction or with those of planetary exploration. The lack of an optical design with a truly 3-D instantaneous FOV is therefore a critical point in modern space plasma instrumentation.

In section 2, we present the basic topology of our "donut" plasma analyzer. Section 3 describes the numerical model of the instrument, and section 4 shows how the constraint of strong UV rejection by the optics is integrated into our design. In section 5, we explain how we optimized the performances of our optical concept and we assess the performances of the numerical model. Our results are summarized in section 6 where we also discuss the perspective of this work.

2. Topology of the 3-D Plasma Analyzer

We present here the basic topology of our 3-D plasma analyzer. Our instrument concept is based on well-known electrostatic optics principles: an electric potential gradient creates an electric field within two curved electrodes [*Dahl*, 1973]. The electric field is oriented toward the center of curvature of the electrodes. The value of the electric potential applied to the electrodes is adjusted to deflect charged particles of a given energy per charge toward the detector at exit of the electrodes. Figure 2 displays a conceptual representation of the 3-D donut analyzer.

Figure 2a shows a top view of the analyzer. It consists of a set of concentric toroidal electrodes that form a number of independent channels. In the specific example displayed here, the optics is composed of nine electrodes defining eight polar angle channels. In Figure 2b which provides a 2-D cut view of the analyzer, the vertical dashed line is the axis of symmetry of the instrument. Azimuthal angles define the direction of incoming
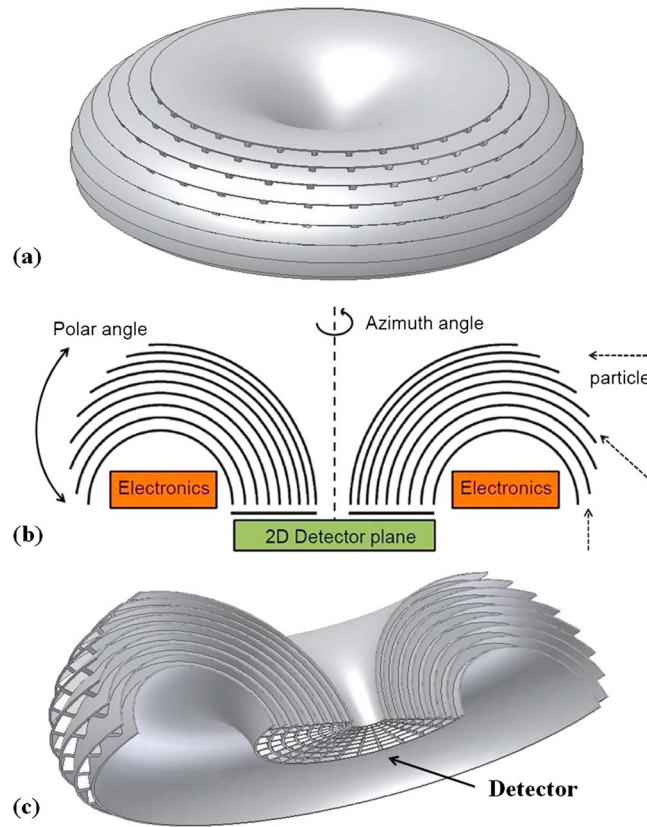
Figure 2. (a) Top view of the 3-D donut analyzer. (b) Cut view with the vertical dashed line as the axis of revolution of toroidal electrodes. Incoming particles of different polar and azimuthal angles are deflected toward the 2-D detector plane. (c) Bottom cut view of the optics showing the location of the 2-D detector.

Figure 3. Sketch of two possible accommodation of the donut analyzer on a satellite. Two sensors are supposed to provide a 4π sr field of view of the surrounding plasma.

particles around this axis. Charged particles coming from the whole hemisphere enter the channels of this donut analyzer and are deflected toward a common imaging detection plane. The location of the detector is visible on the bottom cut view given by Figure 2c. The detection area is a wide planar surface on which the angular distribution of the velocity vector of the detected particle is projected. Polar and azimuthal angles are directly identified by the localization of the particle's impact on the detector. We shall explain in section 5 why we introduce separators between azimuthal sectors. One can also notice that the free space within the half-torus of the innermost electrode may easily be used for electronic modules.

Figure 3 displays possible accommodation of instruments based on this optical concept on a satellite. The two sensor heads that are needed to provide a full 4π sr view of the plasma either can be located on each side of the platform or can form a single unit with two back-to-back heads at the end of a long boom. The choice between these two options would mainly depend upon the specific constraints of the space mission, but, obviously, having a single unit would simplify the technical implementation of the instrument. Since deployable arms create strong dynamical constraints on spin-stabilized spacecraft, the single-unit option would be more appropriate for three-axis stabilized platforms.
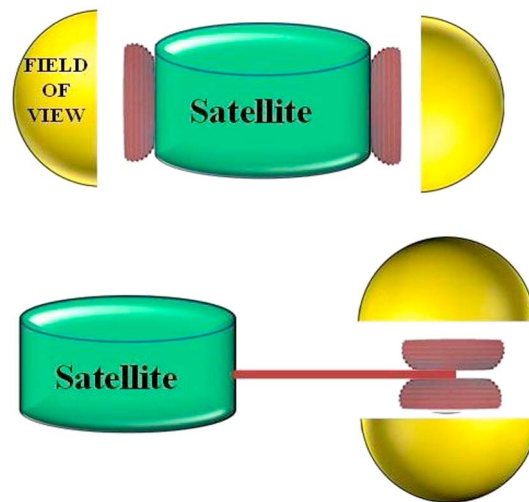
3. Numerical Model

Since the donut analyzer is a complex superposition of many toroidal analyzers, we have developed a numerical model of the electrostatic optics which is fully parametrized and allows an arbitrary number of electrodes to be modeled.

Figure 4 shows a 2-D section in a radial plane of the electrostatic potential for a particular version of the optics with nine electrodes. The main parameters of the optics are the major radius of the tori
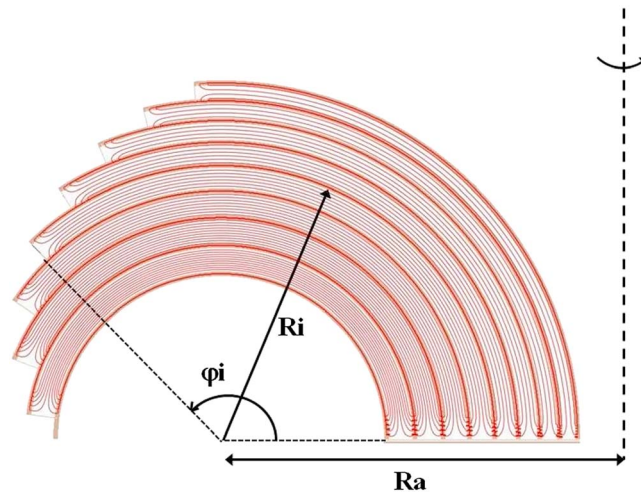
Figure 4. Electrostatic potential 2-D map of a nine-electrode version of the donut analyzer. Major and minor radii of the tori, Ra and Ri ($i \in [1, 9]$), respectively, and the stop angle of the electrodes φ_i are defining the geometry. The vertical dashed line is the axis of revolution of the instrument.

Ra, which is common to all electrodes, the minor radii of individual tori R_i with $i \in [1, N]$, where N is the number of electrodes and $R_{i+1} > R_i$, and the stop angle of the electrodes φ_i. The electrodes thickness has been set to 1 mm. The analyzer is fully determined by these $2N + 1$ parameters. We also introduce in our model individual grounded grids at the entrance of the optics and a planar grid at the exit. In such geometry, the entrance grids have a conical shape. They prevent interferences of electric fields leaking from a channel on the trajectories of particles entering an adjacent channel and, in practice, also allow reducing the volume of the simulation box since the electrostatic potential vanishes outside each entrance grid. The 3-D geometry is described as a 3-D array of binaries with zeroes for free space and ones for electrodes.

A rather classical method to get the entire potential map consists in imposing a given potential V_i to each electrode and, for each set of the analyzer $2N + 1$ parameters, solve the 3-D Laplace equation with appropriate boundary conditions. For clarity, we consider hereafter the case of an ion analyzer. The electric potential should increase from one electrode to the next one $V_{i+1} > V_i$ with $i \in [1, N - 1]$ in order to keep deflecting ions toward the detector plane. In this case, the so-called K factor of the analyzer, which is the ratio between the analyzed energy and the electrode polarization voltage [see, e.g., *Collinson and Kataria*, 2010], would dramatically decrease from one toroid to the next. Due to the limitations of fast sweeping high-voltage power supplies in space experiments, the instrument would be limited to measuring significantly lower energies. This would not meet the requirement of plasma analyzers on board most space plasma physics missions, with the exception of those which are focused on the measurement of thermal electrons in the solar wind as mentioned in section 1.2. Therefore, we have to find an alternative approach.

The solution is to implement toroidal electrodes made in an insulating material and with their two faces metalized and electrically insulated. In this configuration, as will be shown in section 5, each channel behaves as a usual analyzer and the electrode potentials are kept small enough so that particles up to ~30 keV/q can be detected. The metalization should be such that the end section of each electrode is grounded in order to have continuity with the entrance grids while the other parts of the electrode would be high-voltage biased. At this stage of this study we have assumed that the end part of the metallic coating of the electrodes is resistive over a short length of the order of the gap between electrodes (typically a few millimeters) so that the potential varies linearly in this end part till it reaches the main metalized part where it stays constant and equal to the desired polarization voltage.

Figure 4 shows how the electric potential would be distributed in case each electrode is positively biased on its inner face and negatively biased on its external face. We have checked that the simulation results only weakly depend on the length of the resistive coating. Three-dimensional Laplace equation has been solved with the help of the SIMION software which uses the finite differences method [*Dahl*, 2000]. As a rule of the thumb, we have taken a mesh resolution corresponding to 20 points in the electrode gap which was shown adequate on similar SIMION potential computations in previous instruments. Setting the mesh size equal to 0.1 mm allows proper potential computation for minimum electrode gaps of ~2 mm.

The properties of the instrument are evaluated by simulating particle trajectories in the donut analyzer with polarization voltages that select positive ions around 1 keV/q. These calculations have been carried outside of SIMION: we developed parallel computation tools to launch a large number of particles on a cluster of
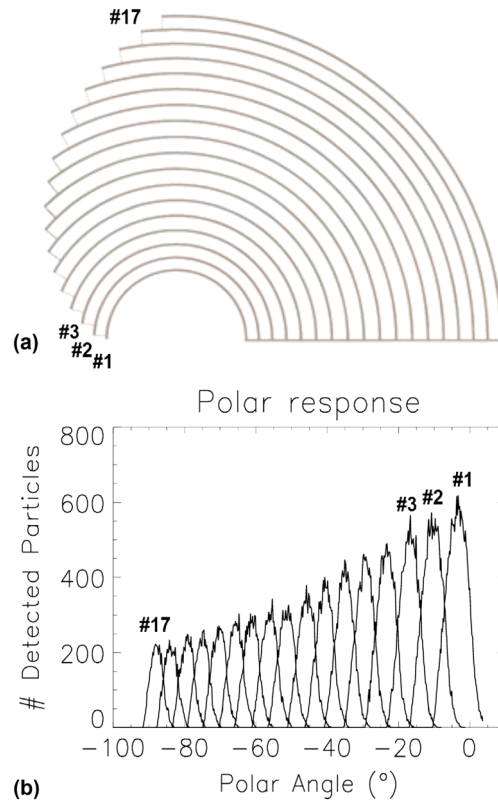
Figure 5. (a) Cylindrical model of the plasma analyzer with 17 channels. (b) Polar response of the plasma analyzer. Geometric parameters of the model are optimized to guarantee efficient UV rejection of the optics together with 50% overlap of the polar response of neighbor channels.

computers which all opened the same electric potential map. Initial positions of the particles are chosen randomly over the entrance window of each channel. The energy of launched particles varies from 0.7 to 1.3 keV with 10 eV steps. For each polar channel, the velocity vector is defined relative to the normal of the entrance grid by the so-called azimuth and polar angles. Simulated azimuth angles are varied from −40° to 40° with respect to normal with 1° steps, while polar angles are varied from −15° to 15° with 0.5° steps. At each time step, the particle position and the velocity vector are derived using the fourth-order Runge-Kutta method. Particles are stopped when they encounter an electrode or when they hit the detector plane that lies 1 mm below the exit grid. Due to the 3-D nature of the optics, we had to launch up to 100 million particles per channel on a computer cluster to fully characterize the instrument.

4. UV Rejection

One of the most important design constraints is to insure that solar UV contamination is strictly less than the typical noise count rate of MCP detectors, i.e., <1 c/s/cm². MCP, which are also used in UV spectrometers, are indeed very sensitive to solar Lyman α emissions at 1215 Å with quantum efficiency ~1% [*Martin and Bowyer*, 1982]. In order to minimize UV access to the inner part of their optics, state-of-the-art instruments use light collimators (see Figure 1) which provide a first bounce on UV-absorbing surfaces. In a top-hat analyzer, the inner surface of the outer sphere can also be scalloped and all internal parts of the optics have to be coated either with black cupric sulfide [*Rème et al.*, 1997] or with black cupric oxide [*Alsop et al.*, 1998]. Taking into account the low integrated hemispheric reflectance of these coatings which is typically a few percent [*Zurbuchen et al.*, 1995], the rule of the thumb is to decrease the interelectrodes gap of the optics such that light rays undergo at least three reflections on black-coated surfaces before hitting the detector. Under these conditions, the typical 3×10^{11}/s/cm² Lyman α photon flux at 1 AU [*Vidal-Madjar*, 1975] is reduced, such that the UV-induced count rate is of the order of the MCP noise count rate. However, reducing the interelectrodes gap limits both the energy acceptance and the angular acceptance of the instrument which finally impacts the sensitivity of the instrument hence its time resolution.

Due to the specific topology of the donut analyzer, we would hardly implement a light collimator at the entrance of the optics and we only rely on black coating of the electrodes. To simplify the part of this initial study focused on UV rejection, we have used a 2-D cylindrical model of the analyzer.

Figure 5a provides the geometry of such a simplified model in the case of an analyzer with 17 polar channels. The innermost channel is defined by its stop angle $\varphi_1 = 180°$ and by its minor radius R_1 which must be large enough to allow the deflection of charged particles up to 30 keV/q with moderate electric fields values, typically less than 2 kV/mm as a safe rule for space instruments that may undergo outgassing which increases somehow the internal pressure compared to the external ultrahigh vacuum. Once (R_1, φ_1) has been set, the radius and stop angle of the second electrode (R_2, φ_2) are chosen to guarantee three reflections of UV
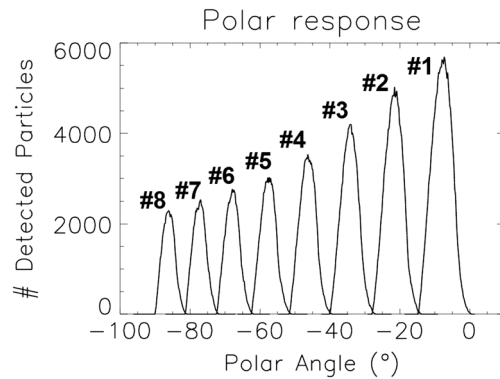
Figure 6. Cylindrical model of the plasma analyzer with eight channels. Geometric parameters of the model are optimized to ensure efficient UV light rejection together with a minimum overlap of the polar response of neighbor channels.

light on the electrodes before photons hit the detector. For a given stop angle φ_2, this condition defines a maximum value for R_2 beyond which UV raypaths with only two reflections on the electrodes can reach the detector. R_2 must decrease with stop angle φ_2. When constructing successive polar channels of the optics, we noticed that there is a single set of parameters (R_i, φ_i) which corresponds to the overlap of the polar response of adjacent channels at a given fraction of their maximum value. The polar response of the optics is given by Figure 5b in the case where the polar responses of neighbor channels overlap at 50% of their maximum.

However, an optics that would provide such an ideal FOV in the polar dimension would correspond in 3-D to a large donut analyzer with ~40 cm diameter. In order to limit the volume and mass of the optics, we used the same approach to optimize the 2-D model of the analyzer for a minimum overlap of the polar response of neighbor channels at ~1% of their maximum. Figure 6 displays the polar response of such an instrument with eight channels. This compact (28 cm diameter, 6 cm height) version of the analyzer corresponds to the parameters used in Figure 2.

In the case of an electron analyzer, another environmental effect is the impact of high-energy electrons that produce substantial amount of electron secondaries which perturb low-energy measurements. In a top-hat configuration, a ring baffle can be designed to trap high-energy particles and electron secondaries at the entrance of the electrostatic analyzer [see, e.g., *Alsop et al.*, 1998]. Using microfabrication techniques, a similar baffle system could be developed to prevent contamination of low-energy electron measurements.

5. Performances of the 3-D Model

5.1. Azimuthal Acceptance and Separators

In order to establish the performances of the 3-D model, we first performed a simulation in which we launched an ion beam parallel to the normal of the entrance surface of the analyzer at a reference point in space. Particle energy and polar angle are swept, and we uniformly scan the entrance of the analyzer over ±20° in azimuth relative to the reference point. All eight channels are illuminated. The major radius of the tori is set to $Ra = 100$ mm, while other parameters are derived from the optimized cylindrical model defined in section 4. Figure 7 shows a scatterplot of particles which reach the (X, Y) detector plane.
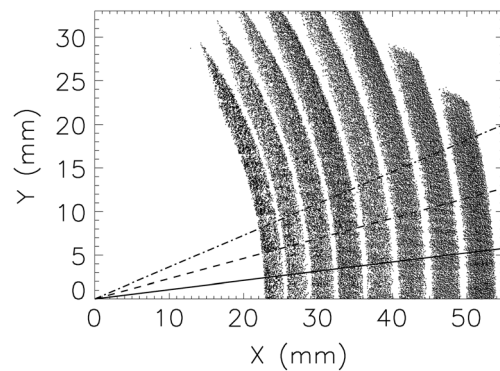

Figure 7. Scatterplot of particles reaching the detection plane after being launched as a beam illuminating the entrance surface of the 3-D analyzer in the $-X$ direction with varying energy and polar angle. Oblique lines intercept the detector at various angles (6°, 13°, and 20°).

The beam is oriented in the $-X$ direction. Only positive Y are represented due to the symmetry of the optics. The rightmost slice of the detected particles corresponds to channel 1 and the leftmost slice to channel 8. An unequal number of particles have been launched in the eight channels to take into account the different sensitivity of the channels and to help visualize the result of this numerical experiment. The oblique plain, dashed, and dash-

Figure 8. Cut view of a single sector of the analyzer showing the electrostatic potential map. Separators are grounded. A transition region between the separators and the main part of the high-voltage biased electrodes is defined where the potential varies linearly.

dotted lines draw a respective angle of 6°, 13°, and 20° relative to the X axis. It shows that the 3-D optics does not focus the parallel ion beam in the azimuthal direction. Instead, the beam is spread over a wide portion of the (X, Y) plane, which means that there will be no way to separate particles with different azimuths with a pixilated detector, whatever the size of the pixel underneath the MCP. This result makes sense since, in the purely toroidal case we considered, the electric field has no component in the azimuthal direction.

As a consequence, we need to introduce physical separators that define a number of sectors in azimuth. The separators will prevent particles with different azimuths to mix in the detection plane. The separators can be seen in Figure 2c. Technically, this modification of the optics has the important impact of potentially connecting electrically toroidal electrodes which should be differentially biased. This apparent contradiction is resolved, in principle, by grounding the separators and by defining a narrow transition region between the separators and the main part of the high-voltage biased electrodes. The issue is the same with the one we faced to have different polarization on the inner and outer faces of each toroidal electrode. The same solution can be considered with the use of selective metalization and of a resistive coating in a transition region between the separators and the main part of the electrodes. The sensitivity of this coating to electric charging when exposed to charged particles will need to be established experimentally. Here again, we assume the length of the transition region to be half the interelectrodes gap (a few millimeters). The electric potential is linearly varying over the transition region as shown in Figure 8. Numerical simulations show that the optics properties only weakly depend on this length.

Next, we studied the role of Ra, the major radius of the tori, in order to optimize its value relative to a target azimuthal resolution of the optics of 12°. This value is typical of electrostatic analyzers for space plasma physics missions. Physical separators are implemented hereafter in our 3-D model as 1° wide grounded planes that intercept the axis of symmetry of the instrument every 13° such that the angular spacing between separators is 12°. Figure 9
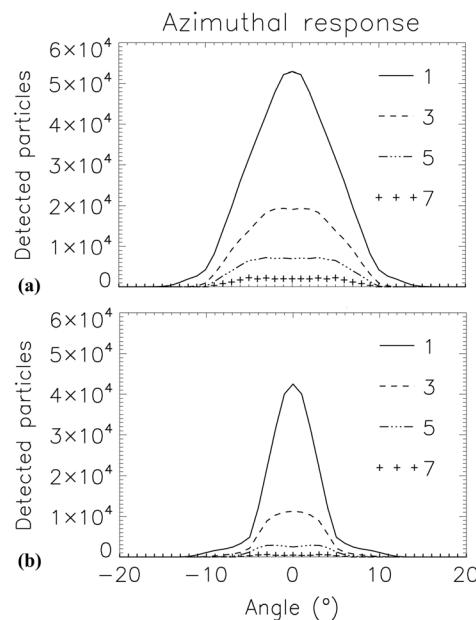

Figure 9. Azimuthal response of four channels of the analyzer with separators between sectors implemented. (a) $Ra = 120$ mm and (b) $Ra = 80$ mm. All possible particle energies, polar and azimuth angles, have been scanned. The 12° wide (in azimuth) entrance of each channel is uniformly illuminated.

Figure 10. Azimuthal response of the optimized eight channels analyzer with $Ra = 100$ mm. All possible particle energies, polar and azimuth angles, have been scanned. The 12° wide (in azimuth) entrance of each channel is uniformly illuminated.
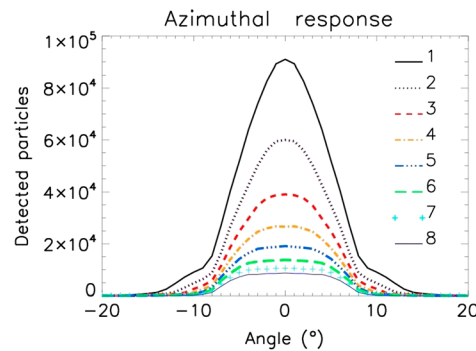
displays the azimuthal response of four of the channels for (a) $Ra = 120$ mm and (b) $Ra = 80$ mm.

To obtain these curves, we uniformly illuminated one sector (in azimuth) of the optics with all possible particle energies (around 1 keV) and all polar and azimuth angles. The total number of detected particles is different for the four channels, which reflects their different sensitivity. For both Ra values, outer channels 5 and 7 have a wider azimuthal FOV than the inner channels 1 and 3. For $Ra = 120$ mm, the azimuthal acceptance of the analyzer $\Delta\alpha$, which can be defined as the full width at half maximum (FWHM) of these curves, reaches 15° for the outer channels while it is 11° and 13°, respectively, for the inner channels 1 and 3. For $Ra = 80$ mm, $\Delta\alpha$ varies from 7° to 11° for channels 1 to 7. We conclude that an optimum value of the major torus of the donut analyzer is of the order of $Ra = 100$ mm.

Figure 10 provides the azimuthal response of the eight channels analyzer for $Ra = 100$ mm. All other parameters (energy, polar, and azimuth angles) as well as the entrance surface of a 12° wide sector in azimuth have been scanned. The simulation has been performed using parallel computing techniques in order to reduce computation time with particles distributed over a large number of processors. The azimuthal acceptance $\Delta\alpha$ varies from ~10° for the first three channels to ~12° for the five outer channels. With such a Ra radius, the optics of the donut analyzer is contained within a 28 cm diameter and 6 cm high cylinder. Such a volume would not be compatible with small cube satellites, but it could easily be accommodated on small satellites.

5.2. Polar Acceptance and Transparency

We now present the results of this 3-D simulation that fully characterizes the optimized eight channels donut analyzer. Figure 11 displays the polar response of the optics. Energy and azimuth angles have been summed up over the whole entrance surface of the channels.

There is no significant difference between these curves and the ones given in Figure 6 which have been obtained in the 2-D case. The polar acceptance of the channels $\Delta\varphi$, which is again defined as the full width at half maximum (FWHM) of these curves, varies from 3° for channel 8 to 6.5° for channel 1, which is similar to the polar acceptance of classical top-hat electrostatic analyzers. We see here the effect of the constraint of UV rejection which induces this inhomogeneous polar acceptance of the channels.
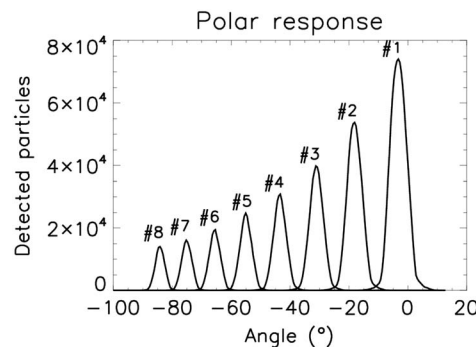

Figure 11. Polar response of the optimized donut analyzer. All possible particle energies, polar and azimuth angles, have been scanned. The entrance of each channel is uniformly illuminated.

Isocontours of the transparency of the optimized analyzer are plotted in Figure 12 as a function of polar and azimuth angles. The transparency (or response function of the analyzer) is defined as the ratio between the effective surface of the analyzer and its entrance surface. At a given energy and for a given velocity vector direction, the effective surface corresponds to the fraction of the entrance surface for which incoming particles eventually reach the detector. Since different channels have different maximum transparency, we have normalized the
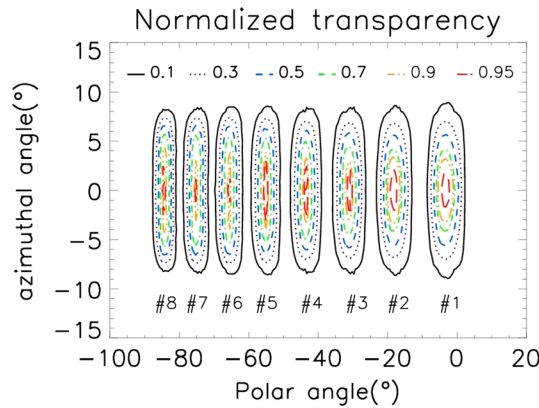
Figure 12. Isocontours of the normalized transparency of the eight channels optimized donut analyzer as a function of azimuth and polar angles. Energies have been summed up, and the whole entrance surface of a single 12° wide sector has been illuminated.

transparency of each channel to its maximum value. Energies have been summed up, and the whole entrance surface of a single 12° wide sector has been illuminated. Figure 12 shows the truly 3-D FOV of the donut analyzer. As expected from Figures 10 and 11, we do observe some minor gaps in the polar response of the channels and a regular coverage of the azimuths.

5.3. Energy Acceptance and Transparency

Figure 13 shows the energy response of the analyzer. Particles with different velocity directions have been summed up. The energy acceptance is the ratio $\Delta E/E$ of the FWHM of these curves ΔE to the mean energy E of detected particles. It is higher for the innermost channels, reaching 10% for channel 1. Outer channels have a lower energy acceptance with 7% for channel 8. The relatively high energy resolution of the donut analyzer would allow a detailed analysis of particle distribution function.

Figure 14 displays isocontours of the normalized transparency as a function of azimuth angle and energy for each channel of the optimized analyzer. Polar angles have been summed up. For outer channels, we observe an asymmetry of the transparency which falls down more rapidly on the high-energy side than on the low-energy one. This is due to the shadowing effect of the tip of the inner electrode of each channel which predominantly affects the highest-energy particles. This contributes to the highest-energy resolution of the outer channels. Practically, the inhomogeneous energy resolution of the optics implies that a trade-off will need to be done when operating the instrument. The high-voltage power supply will need to sweep energies at energy steps that will have to be separated by 7 to 10%.

5.4. Geometric Factor

One of the key quantities that describe the performance of an electrostatic analyzer is its geometric factor G_F. It is a measure of the sensitivity of the optics since the measured particle count rate on the detector is proportional to this quantity through the relation

$$C(E, \alpha, \varphi) = G_F(E, \alpha, \varphi)TJ(E, \alpha, \varphi)q(E), \qquad (1)$$

where T is the measurement time, $J(E,\alpha,\varphi)$ the particle energy differential flux, and $q(E)$ the energy-dependent detector efficiency which differs for electrons [see, e.g., *Collinson et al.*, 2012] and ions [*Fraser*, 2002]. G_F is a function of the particle energy E, the azimuth α, and polar angle φ of its velocity vector, as defined previously.
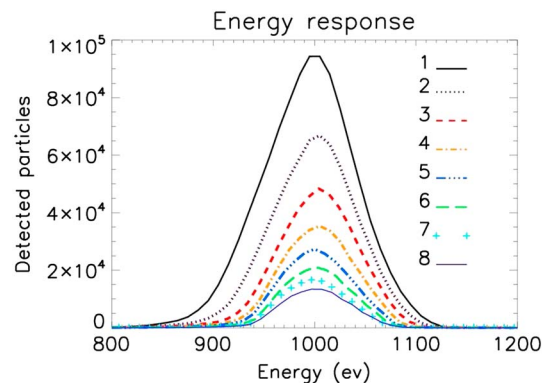

Figure 13. Energy response of the optimized donut analyzer. Particles with different polar and azimuth angles have been summed up. The entrance of each channel is uniformly illuminated.
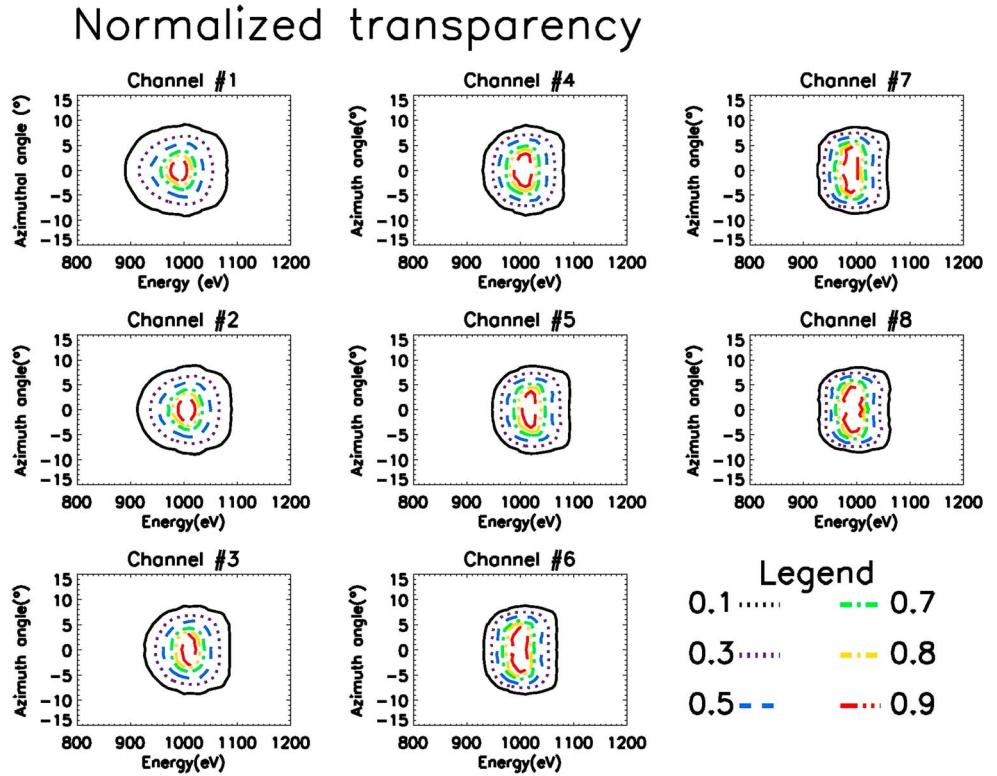
Normalized transparency

Figure 14. Isocontours of the normalized transparency of the donut analyzer as a function of azimuth and energy. Polar angles have been summed up, and the whole entrance surface of a single 12° wide sector has been illuminated.

The knowledge of G_F allows the inversion of experimental data $C(E,\alpha,\varphi)$ and the determination of $J(E,\alpha,\varphi)$ which provides an estimate of the particle distribution function $f(E,\alpha,\varphi) = m^2 J(E,\alpha,\varphi)/(2E^2)$ where m is the particle mass. For the 3-D analyzer, the geometric factor is channel dependent. It can be expressed as

$$G_{Fi}(E, \alpha, \varphi) = E^{-2} \int_{X \in A_i} dA_i \int_{Emin}^{Emax} \widetilde{E} d\widetilde{E} \int_{\varphi min}^{\varphi max} d\widetilde{\varphi} \cos^2 \widetilde{\varphi} \int_{\alpha min}^{\alpha max} d\widetilde{\alpha} R_i \left(\widetilde{E}, \widetilde{\alpha}, \widetilde{\varphi}, x \right) \cos^2 \widetilde{\alpha} \qquad (2)$$

where A_i is the entrance surface of channel i and $R_i \left(\widetilde{E}, \widetilde{\alpha}, \widetilde{\varphi}, x \right)$ is the entrance position-dependent response function of the optics. $R_i \left(\widetilde{E}, \widetilde{\alpha}, \widetilde{\varphi}, x \right)$ is nonzero on a restricted domain, and we can limit the energy, polar, and azimuth angle integration domain. The G_F unit is cm^2 sr eV/eV where eV/eV means that it depends both on particle energy and on the energy acceptance of the optics ΔE and more precisely on the ratio $\Delta E/E$.

Equation (1) implies a number of hypotheses, including stationarity and homogeneity of the plasma over the measurement time and over the instrument position. An estimate of the geometric factor can be obtained from numerical simulations. As shown by *Collinson et al.* [2012], the main source of errors in G_F calculation is the limited number of particles that are launched in the optics. That is why, as mentioned in section 3, we used parallel processing to launch up to 100 million particles per channel in order to obtain good statistics. Energy and incoming directions were discretized with 10 eV steps and 0.5° to 1° steps, respectively, while the entrance surface was randomly illuminated with hundreds of particles for each set of values for E, α, and φ. For each particle, $R_i \left(\widetilde{E}, \widetilde{\alpha}, \widetilde{\varphi}, x \right)$ was simply found to be 0 or 1 depending on whether the particle hit the detector or not. We also took into account the shadowing effect of the tip of each electrode which prevents some particles to access the entrance surface of the optics. The advantage of our approach is that we did not rely on approximations that relate G_F to the energy, polar, and azimuthal acceptance of the optics.

Table 1 summarizes the optical performance of the donut analyzer, including the geometric factor per pixel (i.e., per channel and per azimuthal sector) and the channel-dependent K factor of the analyzer. Assuming that it would be mechanically feasible to implement only 24 sectors that are 12° wide in azimuth, we also provide the total geometric factor per channel integrated over 24 sectors. Another key parameter

Table 1. Summary of the Optical Performances of the Donut Analyzer

Channel i	1	2	3	4	5	6	7	8
G_{Fi} (10^{-3} cm^2 sr eV/eV)	2.2	1.4	0.88	0.57	0.37	0.24	0.16	0.10
Maximum transparency	0.84	0.79	0.80	0.66	0.60	0.58	0.49	0.46
$\Delta E/E$ (FWHM)	10	9	8	8	8	8	7	7
$\Delta\alpha$ (FWHM)	10°	10°	10°	12°	12°	12°	12°	12°
$\Delta\phi$ (FWHM)	6.5°	6°	5°	4.5°	4°	4°	3.5°	3°
Entrance surface (mm^2)	107	106	102	93	82	71	59	48
K factor	3.6	4.2	4.8	5.3	5.9	6.6	7.1	7.7

provided by Table 1 is the maximum transparency of each channel and its entrance surface A_i. The transparency (or response function of the analyzer) is a dimensionless quantity defined as

$$T_i(E,\alpha,\varphi) = \int_{X \in A_i} dA_i R_i(E,\alpha,\varphi,x). \tag{3}$$

Its maximum gives a sense of the intrinsic performance of each channel, while the energy and angular acceptances indicate the resolution of the optics with smaller quantities denoting its ability to discretize the distribution function in finer slices.

Table 1 shows that inner channels have a higher geometric factor which decreases from 2.2 10^{-3}cm^2 sr eV/eV for channel 1 to 10^{-4}cm^2 sr eV/eV for channel 8. This is the combination of a number of effects: the higher maximum transparency of inner channels which varies between 0.84 and 0.46, the wider entrance surface of inner channels which decreases from 107 mm^2 to 48 mm^2 and as shown in previous sections the larger energy and polar acceptance of inner channels. Regarding the geometric factor, the larger azimuthal acceptance of outer channels is marginal and does not modify the trend of higher G_F for inner channels. Assuming a double head (e.g., back-to-back heads) sensor, the global geometric factor of the optics can be defined as $G_F = 2.\sum_{i=1}^{8} G_{Fi}$ where G_{Fi} is the total geometric factor per channel (i.e., for 24 sectors). We found that G_F reaches 0.23 cm^2 sr eV/eV. This estimate does not include the MCP efficiency, which is about 65% at 1 keV for electrons [*Collinson et al.*, 2012], and the entrance and exit grid transparency, which can reach 90% per grid. These numbers combine into the $q(E)$ function of equation (1) which divides by a factor ~2 the optics sensitivity.

6. Conclusions

The limited FOV of state-of-the-art 2-D plasma analyzers is one of the most critical difficulties of modern space plasma instrumentation. This barrier needs to be overpassed to envisage the next generation of space plasma physics missions which should accommodate a limited number of highly performing sensors on low-resource demanding satellites. This calls for the development of a truly 3-D FOV plasma analyzer.

In this paper, we presented the first step toward the achievement of this ambitious objective by describing the numerical performances of a donut analyzer that would provide for the first time a 3-D instantaneous FOV of particle (either ions or electrons) phase space with just two sensors in the thermal energy range from a few eV up to ~30 keV. This 3-D optics consists of a set of concentric toroidal electrodes that deflect particles toward a common imaging detection plane. Without additional deflectors, this energy per charge selective optics provides the full 3-D particle distribution through a single energy sweep. We provided a step by step explanation of the design constraints that were applied to our parametric 3-D model in order to optimize the performances of the donut analyzer. The need of strong UV rejection is an important driver since it strongly reduces the entrance surface and polar acceptance of the outer channels, hence their sensitivity. We showed that an eight-polar channel version of the analyzer was providing a minimum overlap of the polar response of adjacent channels. The topology of the optics prevents the focalization of particles in the azimuthal direction which requires the introduction of physical separators between azimuthal sectors in order to prevent particles with different azimuths to mix in the detection plane. These separators, which need to be grounded, have to be electrically decoupled from the main part of the high-voltage biased electrodes. At the same time, the inner and outer surfaces of the toroidal electrodes have to be independently biased in order to keep the polarization voltage of external channels to acceptable values. We suggested the use of a high dielectric

rigidity polymer that would be selectively metalized and partially processed with a resistive coating that would ensure electrical continuity of the electrode surface.

The optimum value of the major radius of the donut analyzer has been found to be $Ra = 100$ mm, which corresponds to an average azimuthal acceptance of 11° and which meets the requirement of many space plasma missions. Assuming 1° wide separators between azimuthal sectors, we provided the optical properties of a 24 azimuthal sectors instrument. The polar acceptance of the optics varies from 3° for outer channel to 6.5° for inner channels, while its energy acceptance increases from 7% to 10%. Figure 12, which provides the normalized transparency of the optics, shows that it is truly 3-D FOV. Using parallel computing techniques to adequately scan particle phase space, we computed the geometric factor of this specific version of the donut analyzer which would be contained within a 28 cm diameter and 6 cm high cylinder. We noted a significant channel to channel variation of this key quantity, from 2.2×10^{-3} cm^2 sr eV/eV for channel 1 to 10^{-4} cm^2 sr eV/eV for channel 8. The total geometric factor of a double-headed instrument was found to be as high as ~0.23 cm^2 sr eV/eV. For reference, the geometric factor per pixel of the Dual Electron Sensor on board the MMS mission has been estimated by numerical simulation as ~9.1×10^{-4} cm^2 sr eV/eV [*Collinson et al.*, 2012]. The four double-headed electron sensors on board MMS that provide a 3-D FOV after multiple deflections include a total of 128 pixels, which leads to a total geometric factor about half the one of the donut analyzer. However, the inhomogeneous geometric factor of our 3-D analyzer limits the possibility to fully take advantage of the high geometric factor of the innermost channels.

The next step of this research, which is the development of a 3-D analyzer prototype, is ongoing. We will address in a future paper the technological aspects of this development, including the production of selectively metalized electrodes.

References

Alsop, C., S. Scott, and L. Free (1998), UV rejection design and performances of the PEACE electrostatic analyzers, in *Measurement Techniques in Space Plasmas: Particles*, edited by R. F. Pfaff, J. E. Borovsky, and D. T. Young, pp. 269–274, AGU, Washington, D. C., doi:10.1029/GM102p0269.

Angelopoulos, V. (2008), The THEMIS mission, *Space Sci. Rev.*, 141, 5–34, doi:10.1007/s11214-008-9336-1.

Baumjohann, W., and R. A. Treumann (1996), *Basic Space Plasma Physics*, Imperial College Press, London.

Bedington, R., D. O. Kataria, and A. Smith (2014), A highly miniaturized electron and ion energy spectrometer prototype for the rapid analysis of space plasmas, *Rev. Sci. Instrum.*, 85, doi:10.1063/1.4865842.

Berthelier, J.-J., et al. (1998), The Dymio ion mass spectrometer of the Mars-96 mission, in *Measurement Techniques in Space Plasmas: Particles*, edited by R. F. Pfaff, J. E. Borovsky, and D. T. Young, pp. 215–220, AGU, Washington, D. C., doi:10.1029/GM102p0215.

Berthomier, M., et al. (2012), Alfvén: Magnetosphere-ionosphere connection explorers, *Exp. Astron.*, 33, 445–489, doi:10.1007/s10686-011-9273-y.

Burch, J. L., T. E. Moore, R. B. Torbert, and B. L. Giles (2016), Magnetospheric Multiscale overview and science objectives, *Space Sci. Rev.*, 199, 5–21, doi:10.1007/s11214-015-0164-9.

Carlson, C. W., D. W. Curtis, G. Paschmann, and W. Michael (1985), An instrument for rapidly measuring plasma distribution functions with high resolution, *Adv. Space Res.*, 2, 67–70, doi:10.1016/0273-1177(82)90151-X.

Carlson, C. W., J. P. McFadden, P. Turin, D. W. Curtis, and A. Magoncelli (2001), The electron and ion plasma experiment for FAST, *Space Sci. Rev.*, 98, 33–66, doi:10.1023/A:1013139910140.

Collinson, G. A., and D. O. Kataria (2010), On variable geometric factor systems for top-hat electrostatic space plasma analyzers, *Meas. Sci. Technol.*, 21, doi:10.1088/0957-0233/21/10/105903.

Collinson, G. A., J. C. Dorelli, L. A. Avanov, G. R. Lewis, T. E. Moore, C. Pollock, and D. O. Kataria (2012), The geometric factor of electrostatic plasma analyzers: A case study from the fast plasma investigation for the Magnetospheric Multiscale mission, *Rev. Sci. Instrum.*, 83, doi:10.1063/1.3687021.

Dahl, D. A. (2000), SIMION for the personal computer in reflection, *Int. J. Mass Spectrom.*, 200, 3–25, doi:10.1016/S1387-3806(00)00305-5.

Dahl, P. (1973), *Introduction to Electron and Ion Optics*, Academic Press, New York.

Desai, M. I., K. Ogasawara, R. W. Ebert, D. J. McComas, F. Allegrini, S. E. Weidner, N. Alexander, and S. A. Livi (2015), An integrated time-of-flight versus residual energy subsystem for a compact dual ion composition experiment for space plasmas, *Rev. Sci. Instrum.*, 86, doi:10.1063/1.4921706.

Ergun, R. E., et al. (2016), The axial double probe and fields signal processing for the MMS mission, *Space Sci. Rev.*, 199, 167–188, doi:10.1007/s11214-014-0115-x.

Fraser, G. W. (2002), The ion detection efficiency of microchannel plates (MCPs), *Int. J. Mass Spectrosc.*, 215, 13–30, doi:10.1016/S1387-3806(01)00553-X.

Horbury, T., et al. (2006), Cross-Scale: A multi-spacecraft mission to study cross-scale coupling in space plasmas, in *Proceedings of the Cluster and Double Star Symposium*, *ESA SP-598*, edited by K. Fletcher, pp. 1–8, ESA Publications, Noordwijk, Netherlands.

James, A. M., et al. (1998), A fast omni-directional ion detector for the study of space plasmas, in *Measurement Techniques in Space Plasmas: Particles*, edited by R. F. Pfaff, J. E. Borovsky, and D. T. Young, pp. 281–285, AGU, Washington, D. C., doi:10.1029/GM102p0281.

Johnstone, A. D., C. Alsop, P. J. Carter, A. J. Coates, A. J. Coker, R. A. Gowen, B. K. Hancock, T. E. Kennedy, P. H. Sheather, and R. D. Woodliffe (1997), PEACE: A plasma electron and current experiment, *Space Sci. Rev.*, 79, 351–398, doi:10.1023/A:1004938001388.

Kivelson, M. G., and C. T. Russel (1995), *Introduction to Space Physics*, Cambridge Univ. Press, Cambridge.

Linder, D. R., et al. (1998), The Cassini CAPS electron spectrometer, in *Measurement Techniques in Space Plasmas: Particles*, edited by R. F. Pfaff, J. E. Borovsky, and D. T. Young, AGU, Washington, D. C., doi:10.1029/GM102p0257.

Marklund, G. T. (2009), Electric fields and plasma processes in the auroral downward current region, below, within, and above the acceleration region, *Space Sci. Rev.*, *142*, 1–21, doi:10.1007/s11214-008-9373-9.

Martin, C., and S. Bowyer (1982), Quantum efficiency of opaque CsI photocathodes with channel electron multiplier arrays in the extreme and far ultraviolet, *Appl. Opt.*, *21*, 4206–4207, doi:10.1364/AO.21.004206.

McFadden, J. P., C. W. Carlson, D. Larson, M. Ludlam, R. Abiad, B. Elliott, P. Turin, M. Marckwordt, and V. Angelopoulos (2008), The THEMIS ESA plasma instrument and in-flight calibration, *Space Sci. Rev.*, *141*, 277–302, doi:10.1007/s11214-008-9433-1.

Orsini, S., S. Livi, K. Torkar, S. Barabash, A. Milillo, P. Wurz, A. M. Di Lellis, and E. Kallio (2010), SERENA: A suite of four instruments (ELENA, STROFIO, PICAM and MIPA) on board BepiColombo-MPO for particle detection in the Hermean environment, *Planet. Space Sci.*, *58*, 166–181, doi:10.1016/j.pss.2008.09.012.

Paschmann, G., et al. (1985), The plasma instrument for AMPTE IRM, *IEEE Trans. Geosci. Remote Sens.*, *23*, 262–266, doi:10.1109/TGRS.1985.289525.

Pollock, C., et al. (2016), Fast plasma investigation for Magnetospheric Multiscale, *Space Sci. Rev.*, *199*, 331–406, doi:10.1007/s11214-016-0245-4.

Rème, H., et al. (1997), The Cluster ion spectrometry (CIS) experiment, *Space Sci. Rev.*, *79*, 303–350, doi:10.1023/A:1004929816409.

Sauvaud, J.-A., et al. (2008), The IMPACT solar wind electron analyzer (SWEA), *Space Sci. Rev.*, *136*, 227–239, doi:10.1007/s11214-007-9174-6.

Scudder, J., et al. (1995), Hydra—A 3-dimensional electron and ion hot plasma instrument for the POLAR spacecraft of the GGS mission, *Space Sci. Rev.*, *71*, 459–495, doi:10.1007/BF00751338.

Vaisberg, O. L., et al. (1997), Initial observations of fine plasma structures at the flank magnetopause with the complex plasma analyzer SCA-1 onboard the Interball Tail Probe, *Ann. Geophys.*, *15*, 570–586, doi:10.1007/s00585-997-0570-8.

Vaisberg, O. L., et al. (2005), A panoramic plasma spectrometer: An all-sky camera for charged particles, *Cosmic Res.*, *43*, 373–376, doi:10.1007/s10604-005-0058-9.

Vidal-Madjar, A. (1975), Evolution of the solar Lyman alpha flux during four consecutive years, *Sol. Phys.*, *40*, 69–86, doi:10.1007/s10604-005-0058-9.

Wiza, J. L. (1979), Microchannel plate detectors, *Nucl. Instrum. Methods*, *162*, 587–601, doi:10.1016/0029-554X(79)90734-1.

Young, D. T. (1998), Space plasma particle instrumentation and the new paradigm: Faster, cheaper, better, in *Measurement Techniques in Space Plasmas: Particles*, edited by R. F. Pfaff, J. E. Borovsky, and D. T. Young, pp. 1–16, AGU, Washington, D. C., doi:10.1029/GM102p0001.

Zurbuchen, T., P. A. Bochsler, and F. Scholze (1995), Reflection of ultraviolet light at 121.6 nm from rough surfaces, *Opt. Eng.*, *34*, 1303–1315, doi:10.1117/12.199865.